Biochemistry

 Volume 41, Number 39 October 1, 2002

Current Topics

Structural Biology of Viruses by the Combination of Electron Cryomicroscopy and X-ray Crystallography†

Liang Tang and John E. Johnson*

Department of Molecular Biology, The Scripps Research Institute, 10550 North Torrey Pines Road, La Jolla, California 92037

Received February 27, 2002

ABSTRACT: Recent developments in electron cryomicroscopy and image analysis have made it a powerful tool to investigate the structure, assembly, and dynamics of biological supramolecular assemblies. The subjects of study now include a variety of biological samples that may be homogeneous or heterogeneous, symmetric or nonsymmetric. The combination of this technique with X-ray crystallography plays an increasingly important role in structural biology and provides unique structural information for understanding large, complex biological systems. Here we provide an overview of the technologies and specific applications to virus structure and function.

Many biological functions are carried out by complex, multicomponent macromolecular assemblies. The structure, assembly, and dynamics of these molecular machines have long been the focus of biological studies and, due to their unusual complexity, have brought significant challenges and driven innovations to the techniques of structural biology. X-ray crystallography and NMR are still the major methods for providing structural information at atomic detail. Crystallography is the method of choice for the determination of homogeneous structures with high complexity and large sizes, e.g., the 2.4 Å resolution structure of the large subunit and 3.3 Å resolution structure of the small subunit of the ribosome (*1*, *2*), the 2.8 Å structure of yeast RNA polymerase II (*3*, *4*), and the 3.5 Å resolution structures of the bluetongue virus and reovirus cores (*5*, *6*). Over the past 10 years, electron cryomicroscopy and three-dimensional image reconstruction have emerged as a powerful technique in structural biology. Atomic or near atomic models in the resolution range of 3.5−10 Å were obtained for over a dozen integral membrane proteins using ordered two-dimensional arrays (*7*). The typical resolution of structural information derived by single particle cryoEM is currently around 20 Å. Instrumental and computational advancements have, however, improved the resolution beyond 10 Å in some icosahedral viruses by taking advantage of the symmetry. The 7.8 Å resolution cryoEM reconstruction of Hepatitis B virus capsid allowed visualization of secondary structure elements and the protein fold (*8*, *9*), which was confirmed later by the 3.5 Å X-ray structure (*10*). The Herpesvirus capsid, with a diameter of 1250 Å and a molecular weight of ∼0.2 billion, was visualized at 8.5 Å resolution by cryoEM reconstruction (*11*).

The resolution and structural information provided by cryoEM and X-ray crystallography are complimentary. Recently, the combination of these methods has largely expanded our understanding of the structure and function of the biological supramolecular complexes, including the ribosome and complex virus structures. The low-resolution cryoEM model was used to determine the approximate

† We acknowledge grants from the National Institutes of Health (GM34220, GM54076, and AI40101) for support of the authors and work from our laboratory presented in this review.

* Corresponding author. Address: Department of Molecular Biology MB31, The Scripps Research Institute, 10550 North Torrey Pines Road, La Jolla, CA 92037. Phone: 858-784-9705. FAX: 858-784-8660. Website: http://noda.scripps.edu/. E-mail: jackj@scripps.edu.

10.1021/bi020170j CCC: $22.00
Published on Web 08/28/2002

orientation and position of ribosomal subunits in the crystal unit cells of both the large and small ribosomal components, and this information helped locate the heavy atoms required to solve the phase problem in the high-resolution structure determinations (*12*, *13*). The low-resolution cryoEM map of icosahedral virus particles is now routinely used to obtain a set of initial phases for the measured X-ray diffraction intensities. The phases are then refined by noncrystallographic symmetry averaging and phase extension, to solve the high-resolution crystal structures of viruses (for example, ref *14*). A wealth of information on the dynamic nature of domain interactions in complex structures has been obtained by fitting the atomic models from X-ray crystallography into the low-resolution cryoEM maps (*15*).

This review will give a brief introduction to cryoEM and 3D image reconstruction and will focus on recent utilization of these methods in concert in structural studies of viruses which are excellent model systems for biological macromolecular complexes. In-depth descriptions of experimental details of the cryoEM technique have been reviewed (*16*−*20*).

Experimental Method of Cryoem Image Reconstruction. A typical cryoEM reconstruction requires the following steps: flash freezing the sample onto holey EM grids; acquisition of micrographs under low dose condition; image analysis and 3D reconstruction; assessment of quality and resolution; and interpretation and presentation of the structure.

The sample preparation of single particles for cryoEM is straightforward when compared to crystal preparation for X-ray diffraction. A few microliters of sample solution are applied onto a glow-discharged EM grid coated with perforated carbon film. The grid is then blotted with filter paper to remove excess solution, rapidly plunged into liquid ethane slush, and stored in liquid nitrogen. The use of ethane leads to rapid freezing of the sample solution, which vitrifies the sample into a glasslike state and prevents formation of crystalline ice. Such a procedure allows the sample solution to form a thin layer (up to several thousand Ångstroms) in the holes of the grid where the biological objects are evenly distributed. The sample is maintained at liquid nitrogen temperatures with a specially designed cryo specimen holder and is transferred into the electron microscope vacuum for examination. A "good" area is located on the grid at low magnification. To avoid damaging the area used for data collection, alignment of the electron beam and focusing is performed at high magnification in an area adjacent to the one to be photographed. Micrographs are recorded in a low dose mode (5−20 electrons/Å^2) to minimize radiation damage to the macromolecules. Due to the lack of amplitude contrast caused by the small difference in electron scattering between water and biological molecules, images are generated by slightly underfocusing the sample to enhance phase contrast. The image formed, however, is a distortion of the true structure due to the contrast transfer function, a parameter that is characteristic of the particular microscope used, and the data must be corrected for this while creating the high-resolution reconstruction.

Each image of the biological molecule recorded under cryoEM conditions is a 2D projection of 3D density. Many images must be recorded to obtain different views of the object. To reconstruct the native 3D structure from 2D projections, the orientation and position of the different views must be determined. Two approaches have been established to solve this problem: the tilt reconstruction (*21*, *22*) and the common line method (*23*, *24*). In the former approach, successive images are recorded with the sample tilted by defined angles between exposures. Thus, the relative orientation for each view is known. An advantage of the tilting method is that it gives the correct hand for the reconstruction. The common line method assumes the particles in the solution are randomly oriented; hence, the cryoEM images contain many different views of the macromolecule. The Fourier transform of each image corresponds to a central plane of the transform of the 3D object. Since the images are 2D projections of the same 3D object, each pair of them share a common line in the Fourier space, and the angle between their Fourier transforms defines their relative orientation. This reciprocal-space-based approach requires high signal-to-noise ratio for the cryoEM images and is particularly useful when the specimen has high symmetry such as icosahedral viruses.

Once the parameters for the orientation and position of each image are determined, an initial 3D density map is calculated. This initial map is used for subsequent refinement of the orientation and position of the images using model-based methods such as polar Fourier transform (*25*) and cross common line (*26*, *27*). Each 2D image is compared to the predicted projection of the 3D reconstruction, and better parameters of orientation and position are determined for the individual particle projections and a revised 3D map computed. This procedure is iterated to convergence. The resolution of the final reconstruction is typically evaluated by the consistency of the two independent reconstructions, each computed with a randomly split half of the data set (*28*). A variety of software packages are available to visualize, analyze, and present the 3D structure and dynamic information derived from cryoEM (for example, see ref *29*).

CryoEM is also used for structure determination by electron crystallography (*7*). Here, the protein sample is prepared as ordered 2D arrays (2D crystals) by various strategies. Integral membrane proteins can be reconstituted in a synthetic lipid bilayer. Water-soluble proteins will often self-organize as a monolayer by directly adsorbing to a surface or associating with a surface containing ligands that bind to the proteins. CryoEM images are recorded for a sample that is tilted by various angles relative to the electron beam. These images are used to calculate 2D Fourier transforms of the arrays, each corresponding to a central plane of the Fourier transform of the 3D structure. The amplitude and phase information are integrated to compute a 3D map by inverse Fourier transform. In some cases, electron diffraction intensities can be incorporated into the calculation. For highly ordered 2D crystals, cryoEM and image analysis is able to yield 3D structures at near atomic resolution in the membrane plane. Higher resolution is achieved with this method than with single particle approaches because of the large number of molecules in the 2D crystals and their well defined position and orientation in the lattice. Nevertheless, the resolution perpendicular to the membrane plane is significantly lower. This anisotropy in resolution is due to the "missing cone" effect because it

[1] Abbreviations: cryoEM, electron cryomicroscopy; 3D, three-dimensional; 2D, two-dimensional.

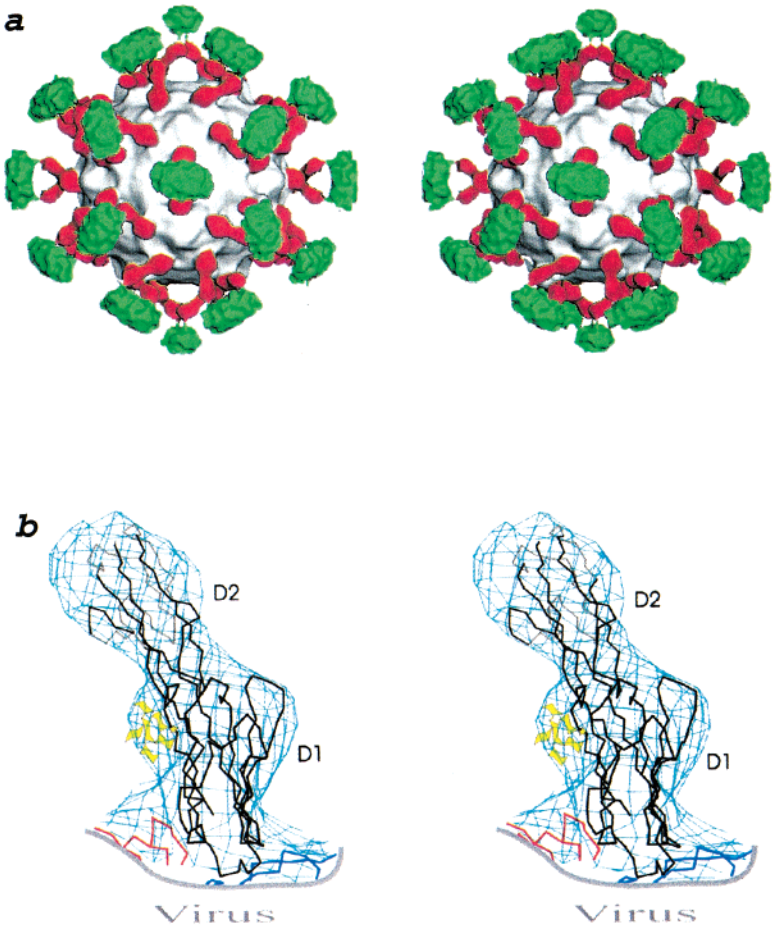

FIGURE 1: (a) Stereoview of the cryoEM map of coxsackievirus−adenovirus receptor (CAR) bound to coxsackievirus B3 (CVB3). The virus is shown as a gray surface. The Ig-like extracellular domains D1 and D2 of CAR are in red, and the transmembrane and cytoplasmic portions of CAR are green. This complex structure may mimic the initial binding state of CVB3 with CAR. Abundant interactions would occur between domain D1 and the virus. In contrast, the transmembrane and cytoplasmic portions are connected to domain D2 by only weak density, suggesting a flexible hinge between them. (b) Stereoview of the Cα trace of CAR D1 and D2 domains (black) fitted into the cryoEM map (light blue). Portions of VP1 (blue) and VP3 (red) of CVB3 are shown. The sugar moiety of the glycosylated Asn108 of domain D1 is indicated by yellow. Figures were adapted from (*43*) with permission.

is not possible to collect images with a tilt angle near 90°; hence, the measured data do not cover the full Fourier space.

CryoEM and image reconstruction of single particles has several advantages over X-ray crystallography. First, there is no special requirement for the purity of the sample, and it is practical to analyze nonhomogeneous samples by manual or computational classification of structurally distinct populations of particles. Hepatitis B coat protein forms two types of icosahedral particles with triangulation numbers $T = 3$ or 4. CryoEM micrographs of the mixed sample were recorded, and images were classified to yield reconstructions at 9 and 11 Å resolution for the two different particles, respectively (*9*). Second, there is no limit to the size of the object. The optimal molecular weight for high-resolution single particle analysis is ∼1−10 MDa. The theoretical lower limit is roughly 100 kDa (*30*). A striking achievement for a small complex is the 10 Å resolution cryoEM structure of U1 small nuclear ribonucleoprotein particle at ∼240 kDa (*31*). Different strategies may allow even smaller objects to be investigated, such as heavy-metallic cluster labeling, binding a small object to a large carrier (e.g., a virus capsid), or difference imaging. Third, the molecule of interest does not need to be crystallized, and it can be an asymmetric single particle or display helical, icosahedral, or other symmetry. Fourth, only a small amount of sample is required and the sample does not need to be at high concentration. For typical viruses, ∼1 mg/mL is sufficient to produce images with enough particles for analysis. Finally, the sample is maintained in a native hydrated form by rapid freezing; thus, the structure obtained represents the state of macromolecule in solution. Flash freezing of the sample also allows time-resolved analysis of transient, functional states of macromolecules with a time resolution at the millisecond level achievable with specially designed spray equipment (*32*). In summary, cryoEM is particularly suitable for studies of large, flexible, nonhomogeneous macromolecular assemblies. The method also allows the investigation of large scale conformational change often associated with biological function, including virus maturation (*33*), genome packaging, membrane fusion (*34*), muscle contraction (*35*), and chaperonin functions (*36*).

Receptors Binding to Viruses. Complexes between viruses and cellular receptors are ideal specimens for study by cryoEM. It is difficult or impossible, in some cases, to create a homogeneous solution of the complex that is completely free of the individual components; therefore, they may be impossible to crystallize. Often, high-resolution structures of each component of the complex have been determined by crystal-

lography. By combining this information with the reconstruction, a wealth of detail may be gained regarding the pattern of molecular interactions between the virus and receptors.

The cryoEM structures of poliovirus type I complexed with the extracellular three-domain receptor (CD155) revealed that the binding site was in a canyon at the poliovirus surface and had a footprint similar to that of binding of major type human rhinoviruses with their receptor, the intercellular adhesion molecule-1 (*37*−*40*). Nevertheless, the relative orientation between the receptors and viruses were remarkably different. The amino acid residues that defined the specificity of recognition also differed. Interestingly, the cellular receptor (very low-density lipoprotein receptor) to human rhinovirus 2 belonging to the minor group bound around the 5-fold vertices of the virus rather than in the canyon (*41*). The similarity in receptor recognition between poliovirus and major group rhinoviruses and the difference between major and minor group rhinoviruses reflect the diversity in adaptability of picornaviruses and may be related to different uncoating mechanisms.

The cryoEM structure of coxsackievirus A21 complexed with the five extracellular domains of its receptor presented a striking view of the virus particle with a radius of 150 Å decorated by the 180 Å long receptors (*42*). The five domains displayed increasing flexibility from the binding domain closest to the virus toward the remote end as the density in the cryoEM map decreased progressively. A first view of interactions between a virus and its full-length receptor was derived by cryoEM for group B coxsackievirus and the coxsackievirus-adenovirus receptor which includes transmembrane and cytoplasmic portions (Figure 1) (*43*).

The outer capsid protein σ1 of reovirus T3D strain binds to the carbohydrate moiety on the surface of host cells, which is critical for viral attachment. Monoclonal antibody to another capsid protein σ3 blocks the binding of σ1 to sialic acid and inhibits reovirus-induced hemagglutination. Binding of reovirus with IgG and Fab was examined by cryoEM (*44*). It was proposed that IgG binding to σ3 leads to steric hindrance for access of the sialic acid binding domain of σ1 whereas Fab did not inhibit HA, which is consistent with immuno-biochemical evidence.

A cryoEM reconstruction of adenovirus in complex with its internalization receptor $\alpha_v\beta$5 integrin and high-resolution crystal structures of foot-and-mouth disease virus-oligosaccharide receptor complexes are also examples of the application of these techniques (*45*, *46*).

Virus Assembly. Lack of icosahedral symmetry and variation in size and shape of the HIV capsid has set back the structural investigation of this enveloped RNA virus. In vitro, recombinant capsid proteins of HIV-1 spontaneously assemble into helical tubes and cones that resemble the virus capsid. Image reconstruction of the helical assemblies of HIV-1 CA proteins at 20−30 Å resolution allowed fitting of the atomic structures of two domains of the capsid protein into the map, showing that the N-terminal domains form the hexameric rings and the C-terminal dimerization domains connect each ring to six neighbors (*47*). A molecular model for the HIV cone structure was proposed in accordance with the principle of a fullerene cone, in which the body of the cone is composed curved arrays of capsid protein hexamers and the narrow and wide ends are closed by inclusion of 5 and 7 pentamers, respectively.

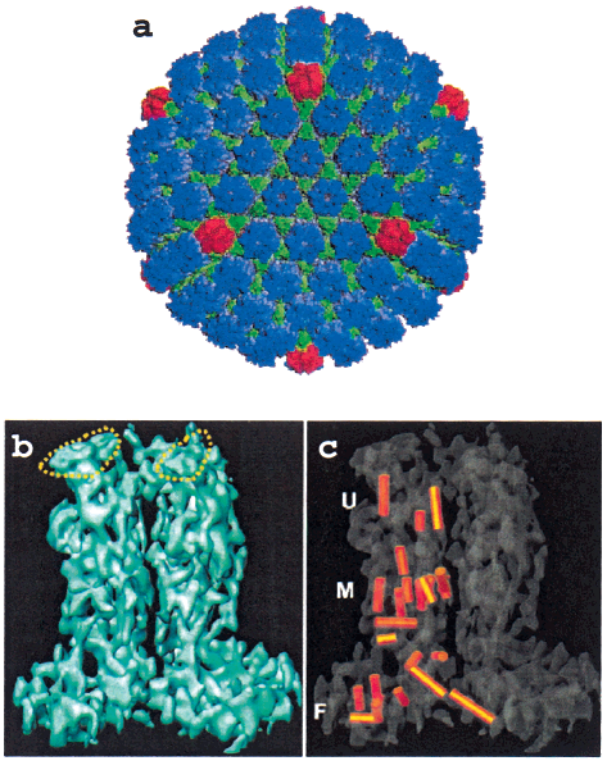

FIGURE 2: (a) Shaded surface view of the 8.5 Å resolution cryoEM structure of $T = 16$ HSV-1 capsid with 12 pentons (red), 150 hexons (blue), and 320 triplexes (green). (b) A side view of two subunits extracted from a 6-fold averaged C hexon. Each subunit consists of a VP5 molecule and a VP26 molecule (dashed lines) on the top of VP5. (c) The same view as panel b with the cryoEM map shown as semitransparent surface. The 24 putative α-helices are shown as gold cylinders (5 Å diameter) in one of the subunits. The upper (U), middle (M), and floor (F) domains of VP5 are indicated. Figures were adapted from (*11*) with permission.

By combining 5860 images of particles from 130 micrographs, cryoEM revealed the structure of human herpes simplex virus type 1 capsid at 8.5 Å resolution (Figure 2) (*11*). This icosahedral capsid is formed by four protein types arranged in a $T = 16$ lattice, with a total molecular mass of 0.2 billion Daltons and a diameter of 1250 Å. More than 30 helices were identified in the density map for the capsid proteins VP5, VP19C and VP23.

Bacteriophage λ has a $T = 7$ capsid encapsidating a linear dsDNA genome. The nucleoprotein head is attached through a connector to a long, flexible tail. The mature capsid is stabilized by binding of a small protein gpD at the 3-fold vertices. The binding sites for gpD are created or exposed only after the prohead expands. The crystallographic trimer in the 1.1 Å resolution X-ray structure of gpD fit well with the thimble-shaped protrusion at the 3-fold axis of the 15 Å resolution cryoEM map of the capsid (*48*). The gpD protein makes contacts with the capsid via a relatively hydrophobic and conservative area where the visible N-terminus (Ser15) is located.

Genome Packaging. Packaging of the viral genome is either a highly cooperative co-assembly of viral proteins and nucleic acids induced by specific and nonspecific interactions or a well-controlled process, which is directed by multiple structural components of the virus requiring a preformed shell. The nucleic acid packaged in the capsid cannot follow the icosahedral symmetry, although it may be organized in

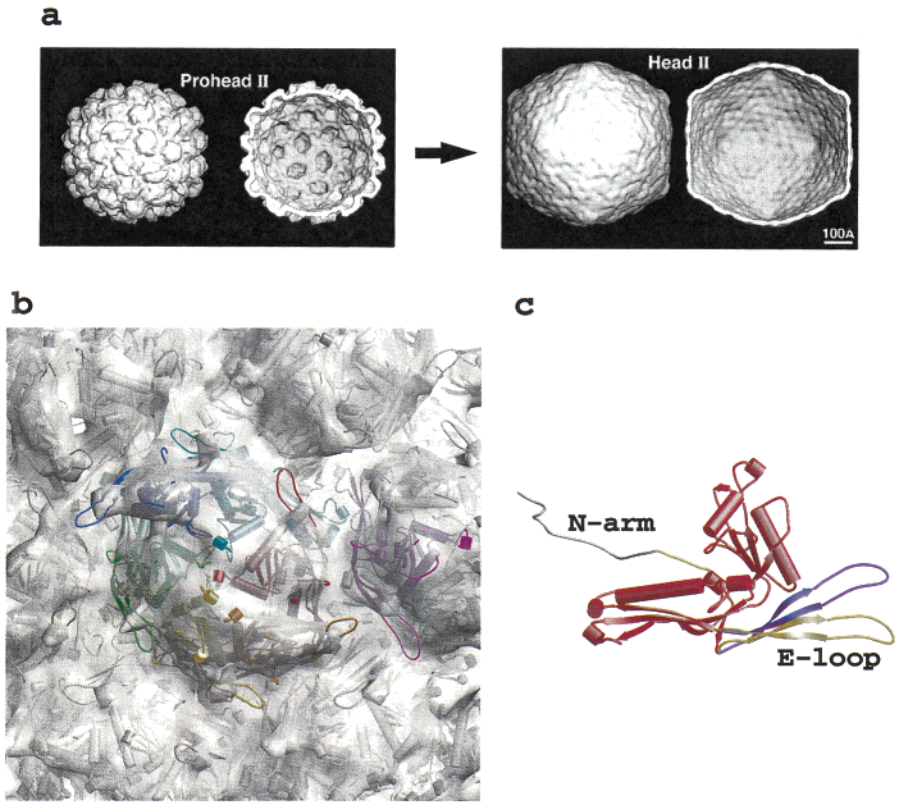

FIGURE 3: (a) CryoEM reconstructions of prohead II (left) and head II (right) of HK97 show dramatic rearrangement of the capsid structure. In both panels: left, top view; right, cutaway view. This figure was adapted from ref *56* with permission. (b) The pseudoatomic model of prohead II derived by fitting subunits in the crystal structure of head II into the cryoEM map of prohead II (semi-transparent surface). Seven subunits in the asymmetric unit are in different colors, and the neighboring subunits are in gray. Subunit rotations between prohead II and head II are as large as 39° with translations as large as 58 Å. A significant portion of the tip of the E-loop protrudes outside the cryoEM density, implying either variation of conformations or disorder of this region in prohead II. (c) Local refolding of the subunit during the transition from prohead II to head II. The E-loop is more hinged in prohead II (purple) than in head II (yellow). The gray portion of the N-arm was omitted in the prohead II model due to steric clash, indicating different folding than that in head II.

a specific form that is required for the next step of the virus life cycle, e.g., replication and/or translocation of the nucleic acid across a membrane.

The crystal structure of the head−tail connector of the bacteriophage ϕ29 was determined at 3.2 Å resolution using a low-resolution cryoEM map from 2D arrays of the connector proteins, and the derived atomic model was readily fitted into the cryoEM maps of the prohead and partially DNA-filled prohead (*49*). The structural components of the connector are proposed to comprise a rotary motor with the prohead RNA-ATPase complex acting as a stator, the DNA acting as a spindle, and the connector as a ball-race. The helical nature of the DNA converts the rotary movement of the connector into translation of the DNA.

The dsRNA genome of bluetongue virus is packaged into spherical shells that were observed in the X-ray electron density at 3.5 Å resolution. The RNA forms spirals putatively associated with transcriptional enzyme complexes near the 5-fold vertices of the capsid, facilitating RNA replication (*50*). Concentric layers of packaged nucleic acids were observed by cryoEM in dsDNA bacteriophage p22, herpes simplex virus, and two dsRNA viruses of the *reoviridae* family, demonstrating striking similarity in the genome organization of these viruses (*51*−*54*).

The amount of packaged genome directs the in vivo assembly of brome mosaic virus capsid proteins into two different surface lattices: a 180-subunit capsid ($T = 3$) encapsidating the natural BMV genomic RNA, which is indistinguishable from authentic virions, and a 120-subunits capsid packaging an engineered mRNA containing only the BMV capsid protein gene (*55*). Modeling of the capsid protein structure from the closely related CCMV into the cryoEM maps of the two capsids suggested that assembly of the $T = 1$ particle with a dimer in the icosahedral asymmetric unit may exploit dramatically different coat protein interactions as well as interactions similar to those in the $T = 3$ particle. This also demonstrated the versatility of capsid protein in particle assembly.

Capsid Maturation. Virus capsid maturation is a common process during assembly of many bacteriophages and some animal viruses. The irreversible transition from the procapsid to the mature capsid involves remarkable physicochemical changes, including dramatic expansion of the particle, dissociation of scaffolding proteins, binding of accessory proteins, rearrangement of the capsid proteins, and/or covalent cross-linking between capsid proteins by auto-catalysis.

HK97, a dsDNA bacteriophage, provides an excellent example for structural studies on capsid maturation (Figure 3). A single-chain 385-residue coat protein forms the earliest precursor, prohead I, which is converted to prohead II by proteolysis of the N-terminal 102 residues of the coat protein. Prohead II then expands by as much as 25% into head I, which produces the mature capsid, head II. A series of intermediates during maturation from prohead I to head II

were captured and imaged by cryoEM (*56*). The X-ray structure of the mature capsid, head II, revealed the topology of the catenated cross-linking between residues K169 and N356 from adjacent subunits. This chain-mail organization of subunits maintains the stable, large capsid (diameter 660 Å) with a remarkably thin shell of proteins (thickness 18 Å) (*57*). Indeed, the structure has been referred to as a molecular balloon. Insights into particle maturation were obtained when the coat protein model from the crystal structure of the head was docked into the cryoEM map of the prohead II at 12 Å resolution. The modeling and comparison of prohead and head revealed that large subunit rotations and translations as well as local refolding accounted for the dramatic change in size and morphology between prohead and head.

Exceptional insights were also obtained from the cryoEM structures of the nucleocapsid, nucleocapsid core, procapsid, and two recombinant particles of the enveloped dsRNA bacteriophage ϕ6. These studies revealed the maturation pathway of this multicomponent machine for RNA packaging and polymerization (*58*).

Change of pH and metal ion concentration reversibly drives the native CCMV particle into a 15% larger swollen form where the quaternary structures of the hexamer and pentamer remain essentially unchanged while the quasi-3-fold axes dramatically expand generating large holes in the particle surface (*59*). Maturation of NωV, a simple ssRNA virus, involves large rearrangements in tertiary and quaternary structure of the coat protein subunits, which may be related to electrostatically driven repositioning of internal helices (*33*). Detailed movements of the subunits were mapped by fitting the atomic model of the capsid, determined by crystallography, into the cryoEM density of the procapsid (*33*).

Membrane Fusion/Penetration. Enveloped viruses carry glycoproteins at the capsid surface that are responsible for receptor recognition and entry into host cells through membrane fusion. However, membranes and glycosylation cause exceptional difficulties for crystallization of the whole viruses. Docking the high-resolution X-ray structure of components into the low-resolution cryoEM map has been a successful strategy to gain knowledge for these viruses. The X-ray structure of the fusion glycoprotein E1 of Semliki forest virus was fitted into the 9 Å resolution cryoEM map of the whole virus, and the result implied flexibility in its domain organization (*34*, *60*). The fusion protein also contributed to the virus assembly through its lateral interactions at the 5-fold and local 2-fold and 6-fold axes and may play a role in virus budding by introducing necessary curvature on the virus surface. Similar organization of transmembrane proteins was observed in Dengue virus (*61*) and a recombinant subviral particle from tick-borne encephalitis virus (*62*).

Reovirus, a nonenveloped animal virus, enters host cells by membrane penetration instead of membrane fusion. The X-ray structure of the membrane-penetration protein μ1 of reovirus T1L strain complexed with its "protector" protein σ3 was recently determined (*63*). Fitting of this heterohexameric complex into the cryoEM map of the whole virion revealed molecular events essential for viral penetration.

The cryoEM reconstruction of the baseplate-tail tube assembly of bacteriophage T4 and the X-ray structure of gp5-gp27 complex, the central part of the baseplate, shed light on an elegant device that punctures the outer cell membrane of *E. coli* and disrupts the intermembrane peptidoglycan layer, allowing ejection of phage DNA into the host (*64*). These structural studies have implications for membrane functions that are regulated by specific proteins in many cellular processes.

Conclusion and Prospects. The combination of X-ray crystallography and cryoEM has had a significant impact on structural biology, and it is driving our understanding of biological mechanisms into a new phase. In the era of structural genomics, X-ray crystallography is moving toward a high throughput mode, and increasingly abundant structural data about individual proteins will be available. It is clear that the majority of cellular proteins function as complexes with other proteins or nucleic acids, and there is more demand for rapid progress in cryoEM technology. Automated procedures for sample preparation and data acquisition on powerful electron microscopes is being established (*65*, *66*). Robust and fast computational algorithms are being developed, and databases are being built for depositing and sharing the structural information from cryoEM. New methods are emerging to dock atomic models into cryoEM maps in a more efficient and quantitative manner with objective validation of the results (*67*−*69*). Moreover, electron tomography enables reconstruction of 3D maps of more polymorphic objects such as mitochondrion (*70*, *71*), Golgi apparatus (*72*), and whole cells (*73*, *74*). The combination of cryoEM, X-ray crystallography, NMR, and other techniques will continue to broaden the type of objects that can be studied. These methods will reveal the functional dynamics of biological systems and, in the long term, establish atomic resolution cell biology by the creative blending of multi-resolution information spanning organizations from atoms, molecules, and molecular assemblage to organelles, cells, and eventually tissues.

ACKNOWLEDGMENT

We thank members of our laboratory for helpful and stimulating discussion.

REFERENCES

1. Ban, N., Nissen, P., Hansen, J., Moore, P. B., and Steitz, T. A. (2000) The complete atomic structure of the large ribosomal subunit at 2.4 Å resolution, *Science 289*, 905−920.
2. Wimberly, B. T., Brodersen, D. E., Clemons, W. M., Jr., Morgan-Warren, R. J., Carter, A. P., Vonrhein, C., Hartsch, T., and Ramakrishnan, V. (2000) Structure of the 30S ribosomal subunit, *Nature 407*, 327−339.
3. Cramer, P., Srebrow, A., Kadener, S., Werbajh, S., de la Mata, M., Melen, G., Nogues, G., and Kornblihtt, A. R. (2001) Coordination between transcription and pre-mRNA processing, *FEBS Lett. 498*, 179−182.
4. Gnatt, A. L., Cramer, P., Fu, J., Bushnell, D. A., and Kornberg, R. D. (2001) Structural basis of transcription: an RNA polymerase II elongation complex at 3.3 Å resolution, *Science 292*, 1876−1882.
5. Grimes, J. M., Burroughs, J. N., Gouet, P., Diprose, J. M., Malby, R., Zientara, S., Mertens, P. P., and Stuart, D. I. (1998) The atomic structure of the bluetongue virus core, *Nature 395*, 470−478.
6. Reinisch, K. M., Nibert, M. L., and Harrison, S. C. (2000) Structure of the reovirus core at 3.6 Å resolution, *Nature 404*, 960−967.
7. Walz, T. and Grigorieff, N. (1998) Electron crystallography of two-dimensional crystals of membrane proteins, *J. Struct. Biol. 121*, 142−161.

8. Böttcher, B., Wynne, S. A., and Crowther, R. A. (1997) Determination of the fold of the core protein of hepatitis B virus by electron cryomicroscopy, *Nature 386*, 88−91.
9. Conway, J. F., Cheng, N., Zlotnick, A., Wingfield, P. T., Stahl, S. J., and Steven, A. C. (1997) Visualization of a 4-helix bundle in the hepatitis B virus capsid by cryo-electron microscopy, *Nature 386*, 91−94.
10. Wynne, S. A., Crowther, R. A., and Leslie, A. G. (1999) The crystal structure of the human hepatitis B virus capsid, *Mol. Cell. 3*, 771−780.
11. Zhou, Z. H., Dougherty, M., Jakana, J., He, J., Rixon, F. J., and Chiu, W. (2000) Seeing the herpesvirus capsid at 8.5 Å, *Science 288*, 877−880.
12. Ban, N., Freeborn, B., Nissen, P., Penczek, P., Grassucci, R. A., Sweet, R., Frank, J., Moore, P. B., and Steitz, T. A. (1998) A 9 Å resolution X-ray crystallographic map of the large ribosomal subunit, *Cell 93*, 1105−1115.
13. Clemons, W. M., Jr., May, J. L., Wimberly, B. T., McCutcheon, J. P., Capel, M. S., and Ramakrishnan, V. (1999) Structure of a bacterial 30S ribosomal subunit at 5.5 Å resolution, *Nature 400*, 833−840.
14. Fry, E. E., Grimes, J., and Stuart, D. I. (1999) Virus crystallography, *Mol. Biotechnol. 12*, 13−23.
15. Rossmann, M. G. (2000) Fitting atomic models into electron-microscopy maps. *Acta Crystallogr., Sect. D: Biol. Crystallogr. 56*, 1341−1349.
16. Frank, J. (1996) Three-Dimensional Electron Microscopy of Macromolecular Assemblies, Academic Press, San Diego.
17. Baker, T. S., Olson, N. H., and Fuller, S. D. (1999) Adding the third dimension to virus life cycles: three-dimensional reconstruction of icosahedral viruses from cryo-electron micrographs, *Microbiol. Mol. Biol. Rev. 63*, 862−922.
18. Thuman-Commike, P. A., and Chiu, W. (2000) Reconstruction principles of icosahedral virus structure determination using electron cryomicroscopy, *Micron 31*, 687−711.
19. van Heel, M., Gowen, B., Matadeen, R., Orlova, E. V., Finn, R., Pape, T., Cohen, D., Stark, H., Schmidt, R., Schatz, M., and Patwardhan, A. (2000) Single-particle electron cryo-microscopy: towards atomic resolution, *Q. Rev. Biophys. 33*, 307−369.
20. Yeager, M., Unger, V. M., and Mitra, A. K. (1999) Three-dimensional structure of membrane proteins determined by two-dimensional crystallization, electron cryomicroscopy, and image analysis, *Methods Enzymol. 294*, 135−180.
21. Amos, L. A., Henderson, R., and Unwin, P. N. (1982) Three-dimensional structure determination by electron microscopy of two- dimensional crystals, *Prog. Biophys. Mol. Biol. 39*, 183−231.
22. Radermacher, M., Wagenknecht, T., Verschoor, A., and Frank, J. (1987) Three-dimensional reconstruction from a single-exposure, random conical tilt series applied to the 50S ribosomal subunit of *Escherichia coli*, *J. Microsc. 146*, 113−136.
23. Crowther, R. A. (1971) Procedures for three-dimensional reconstruction of spherical viruses by Fourier synthesis from electron micrographs, *Philos Trans. R. Soc. London, Ser. B: Biol. Sci. 261*, 221−230.
24. van Heel, M. (1987) Similarity measures between images, *Ultramicroscopy 21*, 95−100.
25. Baker, T. S., and Cheng, R. H. (1996) A model-based approach for determining orientations of biological macromolecules imaged by cryoelectron microscopy, *J. Struct. Biol. 116*, 120−130.
26. Crowther, R. A., Kiselev, N. A., Böttcher, B., Berriman, J. A., Borisova, G. P., Ose, V., and Pumpens, P. (1994) Three-dimensional structure of hepatitis B virus core particles determined by electron cryomicroscopy, *Cell 77*, 943−950.
27. Mancini, E. J., de Haas, F., and Fuller, S. D. (1997) High-resolution icosahedral reconstruction: fulfilling the promise of cryo-electron microscopy, *Structure 5*, 741−750.
28. Grigorieff, N. (2000) Resolution measurement in structures derived from single particles, *Acta Crystallogr., Sect. D: Biol. Crystallogr. 56*, 1270−1277.
29. Conway, J. F., Trus, B. L., Booy, F. P., Newcomb, W. W., Brown, J. C., and Steven, A. C. (1996) Visualization of three-dimensional density maps reconstructed from cryoelectron micrographs of viral capsids, *J. Struct. Biol. 116*, 200−208.
30. Henderson, R. (1995) The potential and limitations of neutrons, electrons and X-rays for atomic resolution microscopy of unstained biological molecules, *Q Rev. Biophys. 28*, 171−193.
31. Stark, H., Dube, P., Luhrmann, R., and Kastner, B. (2001) Arrangement of RNA and proteins in the spliceosomal U1 small nuclear ribonucleoprotein particle, *Nature 409*, 539−542.
32. Fuller, S. D., Berriman, J. A., Butcher, S. J., and Gowen, B. E. (1995) Low pH induces swiveling of the glycoprotein heterodimers in the Semliki Forest virus spike complex, *Cell 81*, 715−725.
33. Canady, M. A., Tihova, M., Hanzlik, T. N., Johnson, J. E., and Yeager, M. (2000) Large conformational changes in the maturation of a simple RNA virus, nudaurelia capensis ω virus (NωV), *J. Mol. Biol. 299*, 573−584.
34. Lescar, J., Roussel, A., Wien, M. W., Navaza, J., Fuller, S. D., Wengler, G., and Rey, F. A. (2001) The Fusion glycoprotein shell of Semliki Forest virus: an icosahedral assembly primed for fusogenic activation at endosomal pH, *Cell 105*, 137−148.
35. Jontes, J. D., and Milligan, R. A. (1997) Brush border myosin-I structure and ADP-dependent conformational changes revealed by cryoelectron microscopy and image analysis, *J. Cell. Biol. 139*, 683−693.
36. Rye, H. S., Roseman, A. M., Chen, S., Furtak, K., Fenton, W. A., Saibil, H. R., and Horwich, A. L. (1999) GroEL-GroES cycling: ATP and nonnative polypeptide direct alternation of folding-active rings, *Cell 97*, 325−338.
37. Belnap, D. M., McDermott, B. M., Jr., Filman, D. J., Cheng, N., Trus, B. L., Zuccola, H. J., Racaniello, V. R., Hogle, J. M., and Steven, A. C. (2000) Three-dimensional structure of poliovirus receptor bound to poliovirus, *Proc. Natl. Acad. Sci. U.S.A. 97*, 73−78.
38. He, Y., Bowman, V. D., Mueller, S., Bator, C. M., Bella, J., Peng, X., Baker, T. S., Wimmer, E., Kuhn, R. J., and Rossmann, M. G. (2000) Interaction of the poliovirus receptor with poliovirus, *Proc. Natl. Acad. Sci. U.S.A. 97*, 79−84.
39. Xing, L., Tjarnlund, K., Lindqvist, B., Kaplan, G. G., Feigelstock, D., Cheng, R. H., and Casasnovas, J. M. (2000) Distinct cellular receptor interactions in poliovirus and rhinoviruses, *EMBO J. 19*, 1207−1216.
40. Kolatkar, P. R., Bella, J., Olson, N. H., Bator, C. M., Baker, T. S., and Rossmann, M. G. (1999) Structural studies of two rhinovirus serotypes complexed with fragments of their cellular receptor, *EMBO J. 18*, 6249−6259.
41. Hewat, E. A., Neumann, E., Conway, J. F., Moser, R., Ronacher, B., Marlovits, T. C., and Blaas, D. (2000) The cellular receptor to human rhinovirus 2 binds around the 5-fold axis and not in the canyon: a structural view, *EMBO J. 19*, 6317−6325.
42. Xiao, C., Bator, C. M., Bowman, V. D., Rieder, E., He, Y., Hebert, B., Bella, J., Baker, T. S., Wimmer, E., Kuhn, R. J., and Rossmann, M. G. (2001) Interaction of coxsackievirus A21 with its cellular receptor, ICAM-1, *J. Virol. 75*, 2444−2451.
43. He, Y., Chipman, P. R., Howitt, J., Bator, C. M., Whitt, M. A., Baker, T. S., Kuhn, R. J., Anderson, C. W., Freimuth, P., and Rossmann, M. G. (2001) Interaction of coxsackievirus B3 with the full length coxsackievirus- adenovirus receptor, *Nat. Struct. Biol. 8*, 874−878.
44. Nason, E. L., Wetzel, J. D., Mukherjee, S. K., Barton, E. S., Prasad, B. V., and Dermody, T. S. (2001) A monoclonal antibody specific for reovirus outer-capsid protein sigma3 inhibits sigma1-mediated hemagglutination by steric hindrance, *J. Virol. 75*, 6625−6634.
45. Chiu, C. Y., Mathias, P., Nemerow, G. R., and Stewart, P. L. (1999) Structure of adenovirus complexed with its internalization receptor, alphavbeta5 integrin, *J. Virol. 73*, 6759−6768.
46. Fry, E. E., Lea, S. M., Jackson, T., Newman, J. W., Ellard, F. M., Blakemore, W. E., Abu-Ghazaleh, R., Samuel, A., King, A. M., and Stuart, D. I. (1999) The structure and function of a foot-and-mouth disease virus- oligosaccharide receptor complex, *EMBO J. 18*, 543−554.
47. Li, S., Hill, C. P., Sundquist, W. I., and Finch, J. T. (2000) Image reconstructions of helical assemblies of the HIV-1 CA protein, *Nature 407*, 409−413.
48. Yang, F., Forrer, P., Dauter, Z., Conway, J. F., Cheng, N., Cerritelli, M. E., Steven, A. C., Pluckthun, A., and Wlodawer, A. (2000) Novel fold and capsid-binding properties of the lambda-phage display platform protein gpD, *Nat. Struct. Biol. 7*, 230−237.
49. Simpson, A. A., Tao, Y., Leiman, P. G., Badasso, M. O., He, Y., Jardine, P. J., Olson, N. H., Morais, M. C., Grimes, S., Anderson, D. L., Baker, T. S., and Rossmann, M. G. (2000) Structure of the bacteriophage phi29 DNA packaging motor, *Nature 408*, 745−750.
50. Gouet, P., Diprose, J. M., Grimes, J. M., Malby, R., Burroughs, J. N., Zientara, S., Stuart, D. I., and Mertens, P. P. (1999) The

highly ordered double-stranded RNA genome of bluetongue virus revealed by crystallography, *Cell 97*, 481−490.
51. Zhang, Z., Greene, B., Thuman-Commike, P. A., Jakana, J., Prevelige, P. E., Jr., King, J., and Chiu, W. (2000) Visualization of the maturation transition in bacteriophage P22 by electron cryomicroscopy, *J. Mol. Biol. 297*, 615−626.
52. Zhou, Z. H., Chen, D. H., Jakana, J., Rixon, F. J., and Chiu, W. (1999) Visualization of tegument-capsid interactions and DNA in intact herpes simplex virus type 1 virions, *J. Virol. 73*, 3210−3218.
53. Zhang, H., Zhang, J., Yu, X., Lu, X., Zhang, Q., Jakana, J., Chen, D. H., Zhang, X., and Zhou, Z. H. (1999) Visualization of protein-RNA interactions in cytoplasmic polyhedrosis virus, *J. Virol. 73*, 1624−1629.
54. Hill, C. L., Booth, T. F., Prasad, B. V., Grimes, J. M., Mertens, P. P., Sutton, G. C., and Stuart, D. I. (1999) The structure of a cypovirus and the functional organization of dsRNA viruses, *Nat. Struct. Biol. 6*, 565−568.
55. Krol, M. A., Olson, N. H., Tate, J., Johnson, J. E., Baker, T. S., and Ahlquist, P. (1999) RNA-controlled polymorphism in the in vivo assembly of 180-subunit and 120-subunit virions from a single capsid protein, *Proc. Natl. Acad. Sci. U. S. A. 96*, 13650−13655.
56. Lata, R., Conway, J. F., Cheng, N., Duda, R. L., Hendrix, R. W., Wikoff, W. R., Johnson, J. E., Tsuruta, H., and Steven, A. C. (2000) Maturation dynamics of a viral capsid: visualization of transitional intermediate states, *Cell 100*, 253−263.
57. Wikoff, W. R., Liljas, L., Duda, R. L., Tsuruta, H., Hendrix, R. W., and Johnson, J. E. (2000) Topologically linked protein rings in the bacteriophage HK97 capsid, *Science 289*, 2129−2133.
58. Butcher, S. J., Dokland, T., Ojala, P. M., Bamford, D. H., and Fuller, S. D. (1997) Intermediates in the assembly pathway of the double-stranded RNA virus phi6, *EMBO J. 16*, 4477−4487.
59. Cheng, R. H., Reddy, V. S., Olson, N. H., Fisher, A. J., Baker, T. S., and Johnson, J. E. (1994) Functional implications of quasi-equivalence in a T = 3 icosahedral animal virus established by cryo-electron microscopy and X-ray crystallography, *Structure 2*, 271−282.
60. Mancini, E. J., Clarke, M., Gowen, B. E., Rutten, T., and Fuller, S. D. (2000) Cryo-electron microscopy reveals the functional organization of an enveloped virus, Semliki Forest virus, *Mol. Cell 5*, 255−266.
61. Kuhn, R. J., Zhang, W., Rossmann, M. G., Pletnev, S. V., Corver, J., Lenches, E., Jones, C. T., Mukhopadhyay, S., Chipman, P. R., Strauss, E. G., Baker, T. S., and Strauss, J. H. (2002) Structure of dengue virus: implications for flavivirus organization, maturation, and fusion, *Cell 108*, 717−725.
62. Ferlenghi, I., Clarke, M., Ruttan, T., Allison, S. L., Schalich, J., Heinz, F. X., Harrison, S. C., Rey, F. A., and Fuller, S. D. (2001) Molecular organization of a recombinant subviral particle from tick- borne encephalitis virus, *Mol. Cell 7*, 593−602.
63. Liemann, S., Chandran, K., Baker, T. S., Nibert, M. L., and Harrison, S. C. (2002) Structure of the reovirus membrane-penetration protein, Mu1, in a complex with is protector protein, Sigma3, *Cell 108*, 283−295.
64. Kanamaru, S., Leiman, P. G., Kostyuchenko, V. A., Chipman, P. R., Mesyanzhinov, V. V., Arisaka, F., and Rossmann, M. G. (2002) Structure of the cell-puncturing device of bacteriophage T4, *Nature 415*, 553−557.
65. Carragher, B., Kisseberth, N., Kriegman, D., Milligan, R. A., Potter, C. S., Pulokas, J., and Reilein, A. (2000) Leginon: an automated system for acquisition of images from vitreous ice specimens, *J. Struct. Biol. 132*, 33−45.
66. Zhu, Y., Carragher, B., Kriegman, D. J., Milligan, R. A., and Potter, C. S. (2001) Automated identification of filaments in cryoelectron microscopy images, *J. Struct. Biol. 135*, 302−312.
67. Roseman, A. M. (2000) Docking structures of domains into maps from cryo-electron microscopy using local correlation, *Acta Crystallogr., Sect. D: Biol. Crystallogr. 56*, 1332−1340.
68. Thouvenin, E., and Hewat, E. (2000) When two into one won't go: fitting in the presence of steric hindrance and partial occupancy, *Acta Crystallogr., Sect. D: Biol. Crystallogr. 56*, 1350−1357.
69. Wriggers, W., Milligan, R. A., and McCammon, J. A. (1999) Situs: A package for docking crystal structures into low-resolution maps from electron microscopy, *J. Struct. Biol. 125*, 185−195.
70. Perkins, G. A., Song, J. Y., Tarsa, L., Deerinck, T. J., Ellisman, M. H., and Frey, T. G. (1998) Electron tomography of mitochondria from brown adipocytes reveals crista junctions, *J. Bioenerg. Biomembr. 30*, 431−442.
71. Mannella, C. A., Buttle, K., Rath, B. K., and Marko, M. (1998) Electron microscopic tomography of rat-liver mitochondria and their interaction with the endoplasmic reticulum, *Biofactors 8*, 225−228.
72. Ladinsky, M. S., Mastronarde, D. N., McIntosh, J. R., Howell, K. E., and Staehelin, L. A. (1999) Golgi structure in three dimensions: functional insights from the normal rat kidney cell, *J. Cell. Biol. 144*, 1135−1149.
73. Baumeister, W., Grimm, R., and Walz, J. (1999) Electron tomography of molecules and cells, *Trends Cell. Biol. 9*, 81−85.
74. McIntosh, J. R. (2001) Electron microscopy of cells: a new beginning for a new century, *J. Cell. Biol. 153*, F25−32.

BI020170J